Imaging with Optical Transition Radiation, Transverse Beam Diagnostics for the XFEL

Gero Kube

- MDI -

March 18, 2008

Abstract

In this note several aspects concerning imaging with optical transition radiation are investigated theoretically. The imaging process is described in the frame of conventional scalar diffraction theory in the sense that the field of an ultra relativistic particle (pseudo photons) is propagated from the source plane, i.e. a metallic target, through a lens to the image plane. Special attention is drawn to the influence of the pre–wave zone effect which in case of high beam energies may influence the imaging properties and as consequence also the resolution. The intention of this note is to sum up the theory described in Refs. [1, 2] in a comprehensive form, and to provide general estimations required for the basic design of an optical transition radiation monitor, especially in view of the XFEL project.

1 Introduction

If a charged particle passes the boundary between two media with different dielectric constants, a broad band electromagnetic radiation is produced which is named transition radiation. The part in the visible range (optical transition radiation or OTR) which is generated at the boundary between a metallic screen and vacuum is widely used for beam diagnostic purposes to measure transverse beam sizes and divergences of charged particle beams like protons [3, 4] or electrons [5, 6, 7, 8] in an electron energy range from 80 keV [9] up to 30 GeV [10]. For the European X–Ray Free–Electron Laser (XFEL) it is also planned to use OTR based profile diagnostics [11]. OTR monitor resolutions has been widely discussed in Refs. [12, 13, 14, 15]. However, in a later work [16] it was demonstrated that the radiation characteristics strongly depends on the distance between source and observation plane similar to the problem of Fresnel resp. Fraunhofer diffraction in classical optics, and the condition for the observation distance a to be located in the so called wave zone can be estimated as $a \gg \lambda \gamma^2$ with λ the wavelength of observation and γ the Lorentz factor. In the case of XFEL with a maximum energy of 20 GeV and a typical optical wavelength $\lambda = 500$ nm the pre–wave zone extends to a distance of ~ 770 m. Having in mind a compact monitor setup the consequence is that the optical elements of the monitor will be located deeply in the pre–wave zone. In Ref. [1, 2] the imaging properties of an OTR beam size monitor were theoretically studied taking into account also the pre–wave zone effect. In this note the theory developed in these references is summarized in a closed form, and general estimations are worked out required for the basic design of a beam size monitor. In order to derive analytical expressions the discussion concerning the monitor resolution is performed in terms of the image of a single particle. For a complete description of the beam image onto the detector this image has to be convoluted with the particle distribution at the screen.

2 Theory

To the authors knowledge with the exception of one monitor design reported in Ref. [17] OTR is usually observed in backward direction, i.e. the radiation appears at specular angle and the target behaves like a mirror. Typically the target inclination angle is $\Psi = 45°$ and consequently the detector is situated under $90°$ with respect to the beam axis. Nevertheless, smaller inclination

angles were also used in order to reduce the depth of field influence [18]. However, in Refs. [19, 20] it was demonstrated that the angular characteristics of backward transition and diffraction radiation of ultra relativistic particles in the wave zone is determined with respect to the mirror reflection direction and does not depend specifically on the target inclination angle Ψ, as far as the condition $\Psi \gg 1/\gamma$ holds.

For the sake of simplicity the task to describe radiation produced from an inclined target is therefore reduced to the case of forward transition radiation and the geometry under investigation is shown in Fig. 1. In this approach the generation of transition radiation is simply considered as reflection
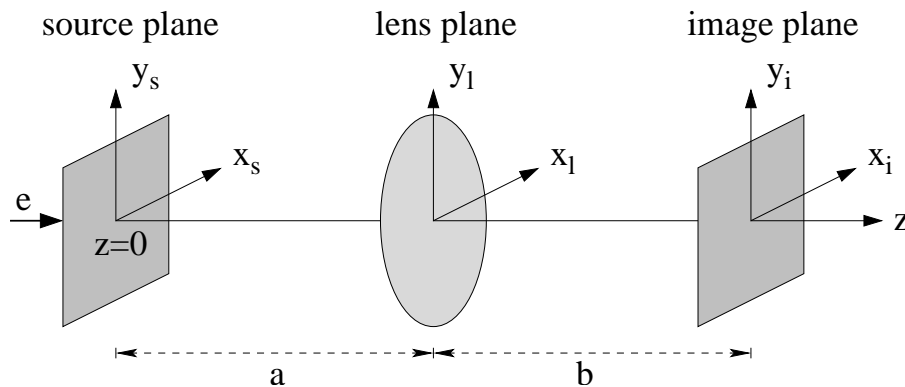

Figure 1: Scheme of the optical system used to calculate the field distribution in the image plane.

of the particle electromagnetic field by the target surface, i.e. the source is represented as pseudo photons which are converted in real photons due to the momentum transfer from the target. It excludes a priori radiation from inside the target itself which can give a significant contribution at higher photon energies [21, 22]. However, in the visible spectral range this contribution is negligible because of self absorption inside the target material. The pseudo photon approach implies a further simplification in the sense that only the transverse field components are considered. In two recent publications [23, 24] the contribution of the longitudinal component was taken additionally into account, allowing an extension of the theory to low particle beam energies and arbitrary inclination angles. This was done either by developing a vector electromagnetic theory for transition and diffraction radiation, or by applying Kirchhoff´s method to a flat target. As it was shown significant differences are to expect if the beam energy is low and/or the target inclination angle is large (i.e. in the case of near grazing incidence). However, these are not the cases under investigation in this note and therefore the application of the simplified pseudo photon method is justified.

2.1 Formulation of the Problem

According to the appendix the source field can be represented in one of the following forms:

$$E^s_{x_s, y_s}(\vec{r}, \omega) = -i \frac{e}{2\pi^2 v} e^{i\frac{\omega}{v}z} \int_{-\infty}^{+\infty} \mathrm{d}^2 k_{x,y} \frac{k_x, k_y}{k_x^2 + k_y^2 + \alpha^2} e^{i(k_x x_s + k_y y_s)} , \tag{1}$$

$$E^s_{x_s, y_s}(\vec{r}, \omega) = \frac{e\alpha}{\pi v} e^{i\frac{\omega}{v}z} \frac{x_s, y_s}{\sqrt{x_s^2 + y_s^2}} \mathrm{K}_1(\alpha\sqrt{x_s^2 + y_s^2}) , \tag{2}$$

$$\text{with} \quad \alpha = \frac{\omega}{\gamma v}.$$

These field representations are standard forms and can be found in many textbooks, see e.g. Ref.[25]. The pseudo photon disc described by these equations has a radial extension with a characteristic value of about $\gamma\lambda$ (see Eq.(57) in the appendix), i.e. even in the case of a single electron the source has a finite size which is strongly increased with increasing beam energy and wavelength.

In the following these scalar fields are propagated through the optical system in Fig. 1. The propagation is treated in the frame of scalar diffraction theory in Fresnel approximation, i.e. up to the quadratic phase term. With the target located at $z = 0$ the propagation from the source plane

to the lens input in a distance a is described by

$$E_{x_l,y_l}^{l_i}(\vec{r_l},\omega) = -i\,\frac{e^{ika}}{\lambda a}\,e^{i\frac{k}{2a}(x_l^2+y_l^2)}\int_{\Sigma_s}\mathrm{d}^2\Sigma_s\,E_{x_s,y_s}^{s}(\vec{r_s},\omega)\,e^{i\frac{k}{2a}(x_s^2+y_s^2)}\,e^{-ik\frac{x_s x_l+y_s y_l}{a}}\;,\qquad(3)$$

see for example Ref. [26]. The integration has to be carried out over the source plane Σ_s.

Before proceeding with the propagation through the optical system a short illustration for the origin of the pre–wave zone will be given. For this it is assumed that the field contributing to the imaging process is originating from an area in the source plane which is given by the finite extension of the pseudo photon disc. With this area an upper limit for the contribution of the quadratic phase factor in Eq.(3) can be given, i.e. for which cases it has to be taken into account or not. To do so the spatial coordinates appearing in that phase which indicates the near field resp. Fresnel diffraction are replaced by the source extension, i.e.the phase is rewritten in the form

$$\exp\left(i\frac{k}{2a}[x_s^2+y_s^2]\right) = \exp\left(i\frac{k}{2a}\rho_s^2\right) = \exp\left(i\pi\frac{\gamma^2\lambda}{a}\right)\;.$$

Inspecting the the quadratic phase term it can be seen that it has to be taken into account if $a \leqslant \gamma^2\lambda$, which is nothing else than the range estimation for the pre–wave zone. At the other hand the contribution can be omitted in the case $a \gg \gamma^2\lambda$, resulting in the wave zone condition.

To study the image formation more in detail the wave propagation through the optical system is continued. In the next step the resulting field Eq.(3) propagates through the lens. In thin lens approximation the effect of the lens is described by introducing an additional quadratic phase shift [26], and the fields at the lens output are given by

$$E_{x_l,y_l}^{l_o}(\vec{r_l},\omega) = E_{x_l,y_l}^{l_i}(\vec{r_l},\omega)\,e^{-i\frac{k}{2f}(x_l^2+y_l^2)}\qquad(4)$$

with f the focal length of the lens.

In the last step the resulting field Eq.(4) propagates from the lens output to the image plane which is situated in a distance b away, see Fig. 1. This propagation is described similar to Eq.(3) and the result reads

$$E_{x_i,y_i}^{i}(\vec{r_i},\omega) = -i\,\frac{e^{ikb}}{\lambda b}\,e^{i\frac{k}{2b}(x_i^2+y_i^2)}\int_{\Sigma_l}\mathrm{d}^2\Sigma_l\,E_{x_l,y_l}^{l_o}(\vec{r_l},\omega)\,e^{i\frac{k}{2b}(x_l^2+y_l^2)}\,e^{-ik\frac{x_l x_i+y_l y_i}{b}}\qquad(5)$$

with the integration performed over the lens surface. Combining these Equations together results in the final representation of the field distribution in the image plane as function of the source and lens properties. However, the variable accessible for a measurement is the intensity in the image plane (detector) which is given by

$$\frac{\mathrm{d}^2W}{\mathrm{d}\omega\mathrm{d}\Omega} = \frac{c}{4\pi^2}\left(|E_{x_i}^{i}|^2 + |E_{y_i}^{i}|^2\right)\;.\qquad(6)$$

The final expression for field and intensity in the image plane depends on the representation of the source field, if either Eq.(1) or Eq.(2) is applied. According to Ref. [2] if the pre–wave zone effect is taken into account the representation by Eq.(2) is better suited while in the far field case the calculation with Eq.(1) is easier to perform. In the following these cases will be considered separately.

2.2 OTR in the Pre–Wave Zone

The combination of Eq.(2) with Eqn.(3)–(5) results in the following representation for the field components:

$$\begin{aligned}
E_{x_i,y_i}^{i}(\omega) =\;& -\frac{e\omega}{\pi\lambda^2\gamma a b v^2}\,e^{ik(a+b)}\,e^{i\frac{k}{2b}(x_i^2+y_i^2)}\int_{\Sigma_l}\mathrm{d}^2\Sigma_l\int_{\Sigma_s}\mathrm{d}^2\Sigma_s\,\frac{x_s,y_s}{\sqrt{x_s^2+y_s^2}}\\
&\times \mathrm{K}_1(\alpha\sqrt{x_s^2+y_s^2})\exp\left(-i\frac{k(x_l x_i+y_l y_i)}{b}\right)\exp\left(i\frac{k(x_s^2+y_s^2)}{2a}\right)\\
&\times \exp\left(-i\frac{k(x_s x_l+y_s y_l)}{a}\right)\exp\left(-i\frac{k}{2}(x_l^2+y_l^2)(1/f-1/a-1/b)\right)\;.
\end{aligned}\qquad(7)$$

3

This expression can be simplified. Firstly it is the intensity which is of interest, therefore according to Eq.(6) the complex exponentials in front of the integral can be omitted. Secondly it will be assumed that the condition for imaging is fulfilled which reads in thin lens approximation

$$\frac{1}{f} = \frac{1}{a} + \frac{1}{b} \; . \tag{8}$$

In this case the last exponential in the integral cancels out and the field is given by

$$
\begin{aligned}
E^i_{x_i,y_i}(\omega) \;=\; & -\frac{e\omega}{\pi\lambda^2\gamma abv^2} \int_{\Sigma_l} \mathrm{d}^2\Sigma_l \int_{\Sigma_s} \mathrm{d}^2\Sigma_s \frac{x_s,y_s}{\sqrt{x_s^2+y_s^2}} \, \mathrm{K}_1(\alpha\sqrt{x_s^2+y_s^2}) \\
& \times \exp\left(-i\frac{k(x_l x_i + y_l y_i)}{b}\right) \exp\left(i\frac{k(x_s^2+y_s^2)}{2a}\right) \exp\left(-i\frac{k(x_s x_l + y_s y_l)}{a}\right).
\end{aligned}
\tag{9}
$$

To proceed further it is suitable to perform the integration in polar coordinates, $x_s = R_s\cos\phi_s$, $y_s = R_s\sin\phi_s$, $x_l = R_l\cos\varphi_l$, $y_l = R_l\sin\varphi_l$, $x_i = R_i\cos\Phi_i$, $y_i = R_i\sin\Phi_i$:

$$
\begin{aligned}
E^i_{x_i,y_i}(\omega) \;=\; & -\frac{e\omega}{\pi\lambda^2\gamma abv^2} \int_0^{\rho_l} \mathrm{d}R_l R_l \int_0^{2\pi} \mathrm{d}\varphi_l \exp\left(-i\frac{k}{b}R_i R_l \cos(\Phi_i - \varphi_l)\right) \\
& \times \int_0^{\rho_s} \mathrm{d}R_s R_s \mathrm{K}_1(\alpha R_s) \exp\left(i\frac{k}{2a}R_s^2\right) \int_0^{2\pi} \mathrm{d}\phi_s (\cos\phi_s, \sin\phi_s) \exp\left(-i\frac{k}{a}R_l R_s \cos(\varphi_l - \phi_s)\right).
\end{aligned}
\tag{10}
$$

The integration over the angles can be carried out directly. Taking into account symmetry considerations and Ref.[27], Eq. 3.915(2) it is

$$\int_0^{2\pi} \mathrm{d}\phi \, (\cos\phi, \sin\phi) \, e^{ix\cos(\Phi-\phi)} = 2\pi i \, (\cos\Phi, \sin\Phi) \, \mathrm{J}_1(x) \tag{11}$$

and the fields in the image plane are given by

$$E^i_{x_i,y_i}(\omega) = \frac{2k^2 e(\cos\Phi_i, \sin\Phi_i)}{\lambda\gamma abv} \int_0^{\rho_s} \mathrm{d}R_s \int_0^{\rho_l} \mathrm{d}R_l \, R_s R_l \, \mathrm{K}_1(\alpha R_s) \, \mathrm{J}_1\!\left(\frac{kR_s R_l}{a}\right) \mathrm{J}_1\!\left(\frac{kR_i R_l}{b}\right) e^{i\frac{k}{2a}R_s^2} \; . \tag{12}$$

According to Refs.[1, 2] dimensionless variables are introduced

$$M = \frac{b}{a}, \qquad \theta = \frac{R_l}{a}, \qquad r_s = k\frac{R_s}{\gamma}, \qquad \zeta = k\frac{R_i}{M}, \qquad \eta = \frac{a}{\gamma^2\lambda} \; . \tag{13}$$

Here M is the magnification of the optical system, θ its collection angle with the maximum acceptance $\theta_m = \rho_l/a$, and η is a measure for the pre–wave zone behavior resp. the Fresnel contribution due to the finite source size. If $\eta \leqslant 1$ the system is in the pre–wave zone, if $\eta \gg 1$ the influence is negligible. With these replacements Eq.(12) reads

$$E^i_{x_i,y_i}(\omega) \;=\; \frac{2e}{\lambda Mv} \, (\cos\Phi_i, \sin\Phi_i) \, f(\theta_m, \gamma, \zeta, \eta) \tag{14}$$

$$\text{with} \qquad f(\theta_m, \gamma, \zeta, \eta) = \gamma \int_0^{\tilde{\rho}_s} \mathrm{d}r_s \, r_s \, \mathrm{K}_1(r_s) \, e^{i\frac{r_s^2}{4\pi\eta}} \int_0^{\theta_m} \mathrm{d}\theta \, \theta \, \mathrm{J}_1(\zeta\theta) \, \mathrm{J}_1(\gamma r_s \theta).$$

The integration over the collection angle can be performed still analytically. With Ref.[28] 11.3.29 and the recurrence relations 9.1.27 therein it is

$$
\begin{aligned}
\int_0^{x_0} \mathrm{d}x \, x \, \mathrm{J}_1(ax) \, \mathrm{J}_1(bx) \;=\; & \frac{x_0}{a^2 - b^2} \left(a \, \mathrm{J}_2(ax_0) \, \mathrm{J}_1(bx_0) - b \, \mathrm{J}_1(ax_0) \, \mathrm{J}_2(bx_0)\right) \\
=\; & \frac{x_0}{a^2 - b^2} \left(b \, \mathrm{J}_1(ax_0) \, \mathrm{J}_0(bx_0) - a \, \mathrm{J}_0(ax_0) \, \mathrm{J}_1(bx_0)\right)
\end{aligned}
$$

4

in accordance with [1], and the final form for the fields in the image plane is obtained:

$$E^i_{x_i,y_i}(\omega) = \frac{2e}{\lambda Mv} \left(\cos \Phi_i, \sin \Phi_i\right) f(\theta_m, \gamma, \zeta, \eta) \tag{15}$$

with

$$f(\theta_m, \gamma, \zeta, \eta) = \gamma \int_0^{\bar{\rho}_s} dr_s \frac{r_s \theta_m \, K_1(r_s) \, e^{i\frac{r_s^2}{4\pi\eta}}}{\gamma^2 r_s^2 - \zeta^2} \left[\zeta \, J_0(\zeta\theta_m) \, J_1(\gamma r_s\theta_m) - \gamma r_s \, J_1(\zeta\theta_m) \, J_0(\gamma r_s\theta_m)\right]. \tag{16}$$

Eq.(16) is the basis for the calculations of OTR taking into account the pre–wave zone contribution.

2.3 OTR in the Far Field

If the condition $\eta \gg 1$ holds, i.e. the lens is in the far field ($a \gg \gamma^2\lambda$), the contribution of the source term $\exp(i\frac{k(x_s^2+y_s^2)}{2a})$ can be additionally neglected. Omitting the complex exponentials in front of the integral in Eq.(7) as before and assuming the condition for imaging in thin lens approximation according to Eq.(8), the fields in the image plane are determined by

$$\begin{aligned} E^i_{x_i,y_i}(\omega) &= \frac{ie}{2\pi^2\lambda^2 abv} \int_{\Sigma_l} d^2\Sigma_l \int_{\Sigma_s} d^2\Sigma_s \int d^2k_{x,y} \frac{k_x, k_y \, e^{i(k_x x_s + k_y y_s)}}{k_x^2 + k_y^2 + \alpha^2} \\ &\quad \times \exp\left(-i\frac{k(x_l x_i + y_l y_i)}{b}\right) \exp\left(-i\frac{k(x_s x_l + y_s y_l)}{a}\right) \end{aligned} \tag{17}$$

which has to be compared with the relevant expression for the pre–wave zone case Eq.(9). The exponentials in this equation can be rearranged

$$\begin{aligned} E^i_{x_i,y_i}(\omega) &= \frac{ie}{2\pi^2\lambda^2 abv} \int_{\Sigma_l} d^2\Sigma_l \int_{\Sigma_s} d^2\Sigma_s \int d^2k_{x,y} \frac{k_x, k_y \, e^{-i\frac{k}{b}(x_i x_l + y_i y_l)}}{k_x^2 + k_y^2 + \alpha^2} \\ &\quad \times e^{i(k_x - kx_l/a)x_s} \, e^{i(k_y - ky_l/a)y_s}, \end{aligned} \tag{18}$$

and keeping in mind the relation for the δ-function

$$\int_{-\infty}^{+\infty} dx_s \, e^{i(k_x - kx_l/a)x_s} \int_{-\infty}^{+\infty} dy_s \, e^{i(k_y - ky_l/a)y_s} = 2\pi\delta(k_x - k\frac{x_l}{a}) \cdot 2\pi\delta(k_y - k\frac{y_l}{a})$$

the integration over the source area and the wave numbers can be carried out:

$$E^i_{x_i,y_i}(\omega) = \frac{ie}{\pi\lambda abv} \int_{\Sigma_l} d^2\Sigma_l \frac{1}{(x_l/a)^2 + (y_l/b)^2 + (1/\beta\gamma)^2} \frac{x_l, y_l}{a} \, e^{-i\frac{k}{b}(x_i x_l + y_i y_l)}. \tag{19}$$

As before it is suitable to perform the integration in polar coordinates, $x_l = R_l \cos\varphi_l, y_l = R_l \sin\varphi_l$, $x_i = R_i \cos\Phi_i, y_i = R_i \sin\Phi_i$. In this case the field can be rewritten in the form

$$E^i_{x_i,y_i}(\omega) = \frac{ie}{\pi\lambda abv} \int_0^{\rho_l} dR_l \frac{R_l^2/a}{(R_l/a)^2 + (1/\beta\gamma)^2} \int_0^{2\pi} d\varphi_l \, (\cos\varphi_l, \sin\varphi_l) \, e^{-i\frac{k}{b}R_i R_l \cos(\Phi_i - \varphi_l)} \tag{20}$$

and the angular integration is performed with Eq. (11), resulting in

$$E^i_{x_i,y_i}(\omega) = \frac{2e}{\pi\lambda abv} \left(\cos\Phi_i, \sin\Phi_i\right) \int_0^{\rho_l} dR_l \frac{R_l^2/a}{(R_l/a)^2 + (1/\beta\gamma)^2} \, J_1(\frac{kR_i R_l}{b}). \tag{21}$$

Introducing the same dimensionless variables Eq.(13) as in the previous section, the fields in the image plane are finally obtained:

$$E^i_{x_i,y_i}(\omega) = \frac{2e}{\lambda Mv} \left(\cos\Phi_i, \sin\Phi_i\right) f(\theta_m, \gamma, \zeta, \eta) \tag{22}$$

with (assuming $\beta = 1$)

$$f(\theta_m, \gamma, \zeta) = \int\limits_0^{\theta_m} \mathrm{d}\theta \; \frac{\theta^2}{\theta^2 + 1/\gamma^2} \; \mathrm{J}_1(\zeta\theta). \tag{23}$$

Eq.(23) is the basis for the calculations of OTR in the far field zone. Comparing the results for far field OTR with the ones taking into account the pre–wave zone effect one can see that the general structure of the fields Eq.(15) resp. Eq.(22) is the same, the difference is represented by the function $f(\theta_m, \gamma, \zeta, \eta)$ which describes the specific properties of the imaging process. Therefore in the following only this part is considered.

According to Ref.[2] the field can be further simplified, keeping in mind that typically the acceptance angle θ_m of the lens is much larger than the OTR cone opening angle, i.e. that $\theta_m \gg 1/\gamma$. In this situation Eq.(23) can be rewritten to a very good precision as

$$f(\theta_m, \gamma, \zeta) \approx \int\limits_0^{\infty} \mathrm{d}\theta \; \frac{\theta^2}{\theta^2 + 1/\gamma^2} \; \mathrm{J}_1(\zeta\theta) - \int\limits_{\theta_m}^{\infty} \mathrm{d}\theta \; \mathrm{J}_1(\zeta\theta), \tag{24}$$

and there exist analytical expressions for both integrals (Ref.[27], Eq. 6.566(2) resp. 6.511(9)):

$$f(\theta_m, \gamma, \zeta) = \frac{1}{\gamma} \mathrm{K}_1(\zeta/\gamma) - \frac{1}{\zeta} \mathrm{J}_0(\zeta\theta_m) = \zeta^{-1} \left[\zeta/\gamma \, \mathrm{K}_1(\zeta/\gamma) - \mathrm{J}_0(\zeta\theta_m) \right]. \tag{25}$$

A further simplification can be performed in the ultra relativistic limit taking into account that $\zeta/\gamma \to 0$, and consequently in this limit $z \, \mathrm{K}_1(z) \to 1$. Therefore in this limit the relation

$$f(\theta_m, \zeta) = \zeta^{-1} \left[1 - \mathrm{J}_0(\zeta\theta_m) \right] \tag{26}$$

holds, i.e. the imaging properties of OTR are independent on the beam energy.

3 Imaging with OTR

To demonstrate the modification of radiation properties in the near field, in a first step the evolution of the wave front from the source is considered. The intensity distribution at the entrance side of the lens is calculated which corresponds to the radiation angular distribution at the location of the lens. Hereafter the OTR imaging properties are studied taking into account the influence of the pre–wave zone. The image of a single particle is calculated according to Eq.(16) and the influence on the resolution is studied. In close analogy to the diffraction limited image distribution of a point source in classical optics (point spread function, PSF) the quantity $|f(\theta_m, \gamma, \zeta, \eta)|^2$ is referred as single particle function (SPF) in the following according to Ref.[15].

3.1 Angular Distribution in the Near Field

Keeping in mind the derivation of the OTR near field image, by inspecting Eq.(14) it can be seen directly that the angular distribution in the lens plane is described by the term

$$f_L(\gamma, \theta, \eta) = \int\limits_0^{\tilde{\rho}_s} \mathrm{d}r_s \; r_s \; \mathrm{K}_1(r_s) \, \mathrm{J}_1(\gamma \, r_s \theta) \; e^{i \frac{r_s^2}{4\pi\eta}}. \tag{27}$$

If the lens is in the far field (i.e. $e^{i \frac{r_s^2}{4\pi\eta}} \to 1$) and the target extensions are assumed to be large enough ($\rho_s \to \infty$) the integration over the source area can be carried out directly taking into account Ref.[27], Eq. 6.521(2). The result reads

$$f_L(\gamma, \theta) = \frac{1}{\gamma} \; \frac{\theta}{\theta^2 + 1/\gamma^2} \; , \tag{28}$$

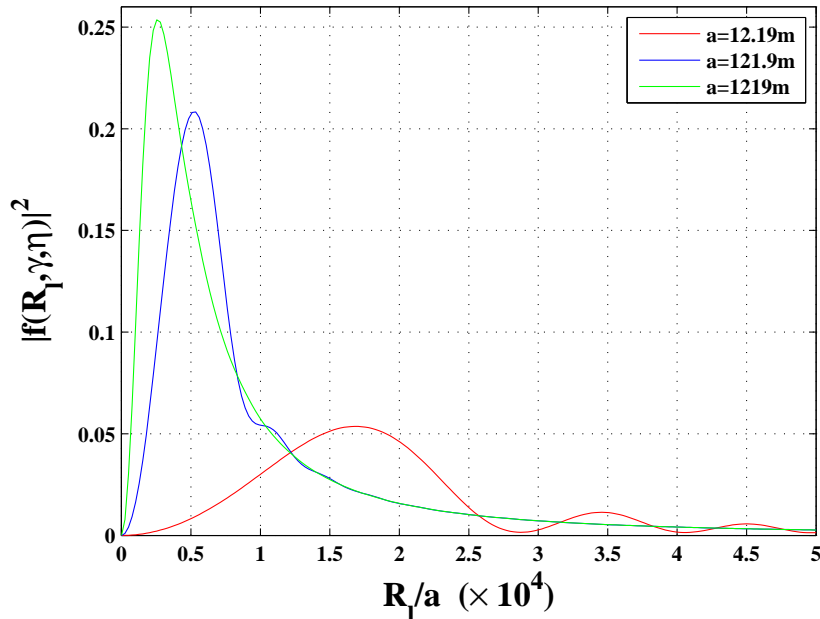i.e. it is the standard far field angular distribution.

Figure 2: OTR near field angular distribution in the lens plane, calculated according to Eq.(27). The parameters were chosen such that they correspond to the calculations with dimensionless parameters in Refs.[1, 16]: $\eta_1 = \frac{0.1}{2\pi}$, $\eta_2 = \frac{1}{2\pi}$, $\eta_3 = \frac{10}{2\pi}$. With the XFEL maximum beam energy of 20 GeV, a typical observation wavelength of $\lambda = 500$ nm, and η determined by Eq.(13) the respective observation distances a are obtained.

In Fig.2 calculations for the angular distribution $|f_L(\gamma, \theta, \eta)|^2$ with f_L according to Eq.(27) are shown. The parameters are chosen such that they correspond to calculations presented in Refs.[1, 16]. As can be seen the angular distribution is strongly affected, even at a distance of about 10 m between lens and target. The consequence is that in the case of an OTR monitor setup for the XFEL the lens is situated deeply in the pre–wave zone.

Taking into account the experience with OTR monitors at FLASH, a reasonable distance would be $a = 0.5$ m which corresponds there to a 1:1 magnification of the optical system [7]. In Fig.3 calculations of the OTR near field angular distribution are shown together with the far field approximation for various beam energies. For smaller beam energies the angular near field distribution approaches the form of the far field approximation. Fig.4 shows again the near field angular distribution for the same parameters and the XFEL maximum beam energy of 20 GeV, but over a wider range in the lens plane.

From the figures presented it is clear to see that the angular distribution exhibits a strongly oscillating structure which is drastically broadened in comparison to the far field approximation. Furthermore it is also important to note that the location of the first maximum remains unchanged in all cases and does not coincide with the far field maximum $1/\gamma$.

Following the discussion in Ref.[1] the position of this maximum can be estimated by inspecting Eq.(27). Keeping in mind that the function $r_s \, \mathrm{K}_1(r_s)$ is continuously decreasing while $\mathrm{J}_1(\gamma \, r_s \theta)$ and $\exp(i\frac{r_s^2}{4\pi\eta})$ exhibit an oscillatory behavior, and that $\mathrm{J}_1(\gamma \, r_s \theta)$ is a real function, the integral in Eq.(27) achieves its maximum at a value R_{l0} in the lens plane where the overlap between both oscillating functions is maximal. This condition can be reformulated such that the zeroes of $\Re[\exp(i\frac{r_s^2}{4\pi\eta})]$ and $\mathrm{J}_1(\gamma \, r_s \theta)$ coincide, i.e.

$$\frac{r_s^2}{4\pi\eta} = \frac{\pi}{2} \qquad \text{and} \qquad \gamma \, r_s \theta_0 = 3.8317 \, .$$

Resolving for $\theta_0 = R_{l0}/a$ and rewriting the condition in physical variables rather than in dimensionless ones results in the position of the first maximum in the lens plane

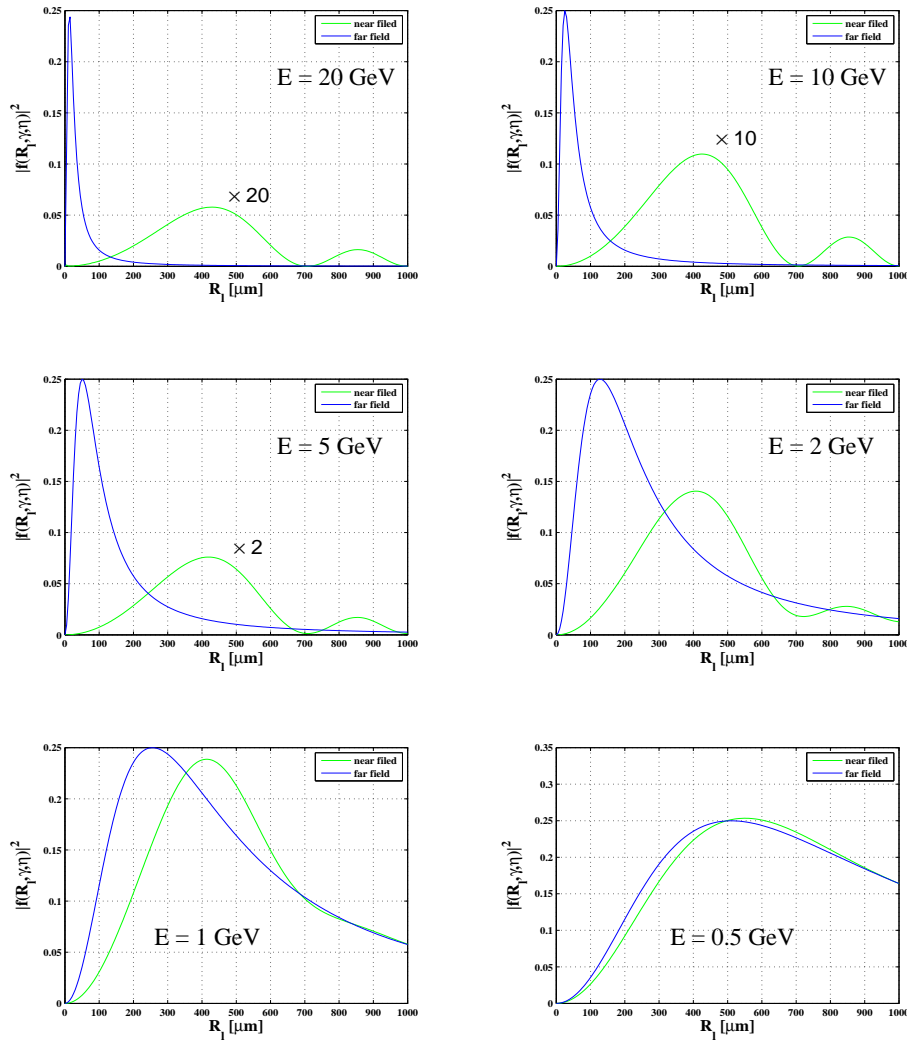$$R_{l0} \approx 0.8624 \, \sqrt{a\lambda} \, . \tag{29}$$

7

Figure 3: Comparison of the OTR near field angular distribution in the lens plane Eq.(27) with the far field distribution Eq.(28) for various beam energies. Parameters of calculation: $a = 0.5$ m and $\lambda = 500$ nm.
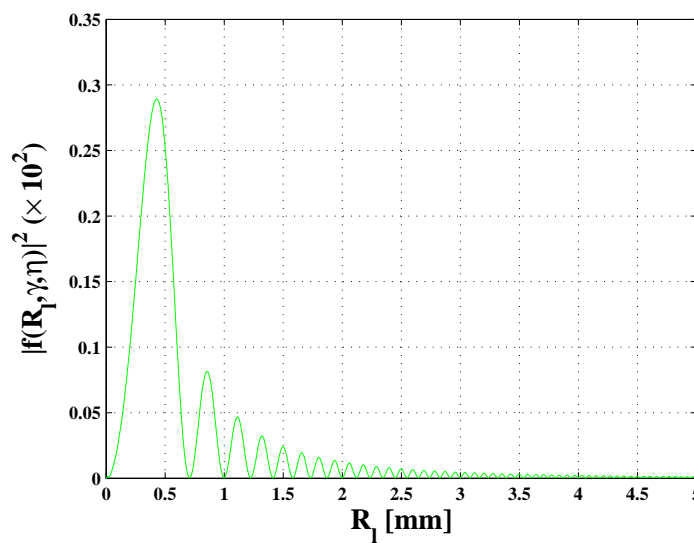

Figure 4: OTR near field angular distribution in the lens plane ($a = 0.5$ m) for a 20 GeV electron beam and an observation wavelength of $\lambda = 500$ nm.

8

This condition is indeed independent on the particle beam energy and the value of $R_{l0} = 431$ μm coincides very good with the calculations as presented in Figs.3,4.

3.2   OTR Imaging in the Pre–Wave Zone

After the demonstration that the OTR angular distribution strongly depends on the distance from the source to the observation point and that for a reasonable monitor size in case of XFEL diagnostics the lens will be deeply located in the pre–wave zone, now the SPF in the image plane is investigated for various cases. Basis for the calculations of image generation in this section is Eq.(16) for the near filed case and Eqn.(23), (25) for the far field resp. the approximative far field case.

Fig.5 shows calculated SPFs in the image plane taking into account the near field contribution. The parameters correspond to the ones of Fig.2 for the angular distributions. In order to keep the lens aperture θ_m constant the lens diameter was scaled in the same way than the distance a between target and lens. While in the case of the angular distribution the near filed effects are clearly visible, in the case of imaging the curves for various distances coincide perfectly, i.e. the influence of the pre–wave zone effect is negligible as already assumed in Ref.[15].
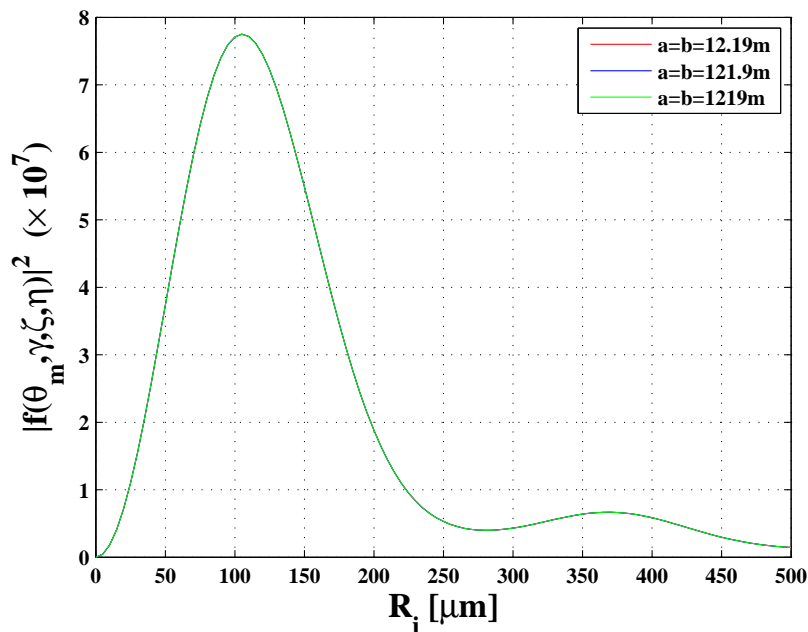

Figure 5: OTR near field image according to Eq.(16). The parameters correspond to the ones of Fig.2. The optical system was assumed to perform a 1:1 imaging, and the lens aperture θ_m was kept constant assuming a lens diameter of $\oslash$ 50.8 mm for the minimum distance of $a = 12.19$ m.

In order to study the pre–wave zone influence more in detail and to compare with the far field calculations Eqn.(23) and (25), Fig.6 shows various calculations for a 1:1 optical imaging system (i.e. $a = b$) with the distance a between source and lens as parameter. Similar as before the lens aperture θ_m is kept constant, i.e. with varying distance a the lens diameter is scaled in the same way. As can be seen only at very small distances far away from to be realistic for an imaging system the pre–wave zone effect influences the image formation. From these calculations it can be concluded that near field contributions are negligible with parameters realistic for the XFEL. Furthermore it can be seen that the accuracy of the approximative far field calculation Eq.(25) is sufficient to describe the image formation for the parameters under investigation here. As consequence in the following sections the calculations are restricted to the case of far field imaging.
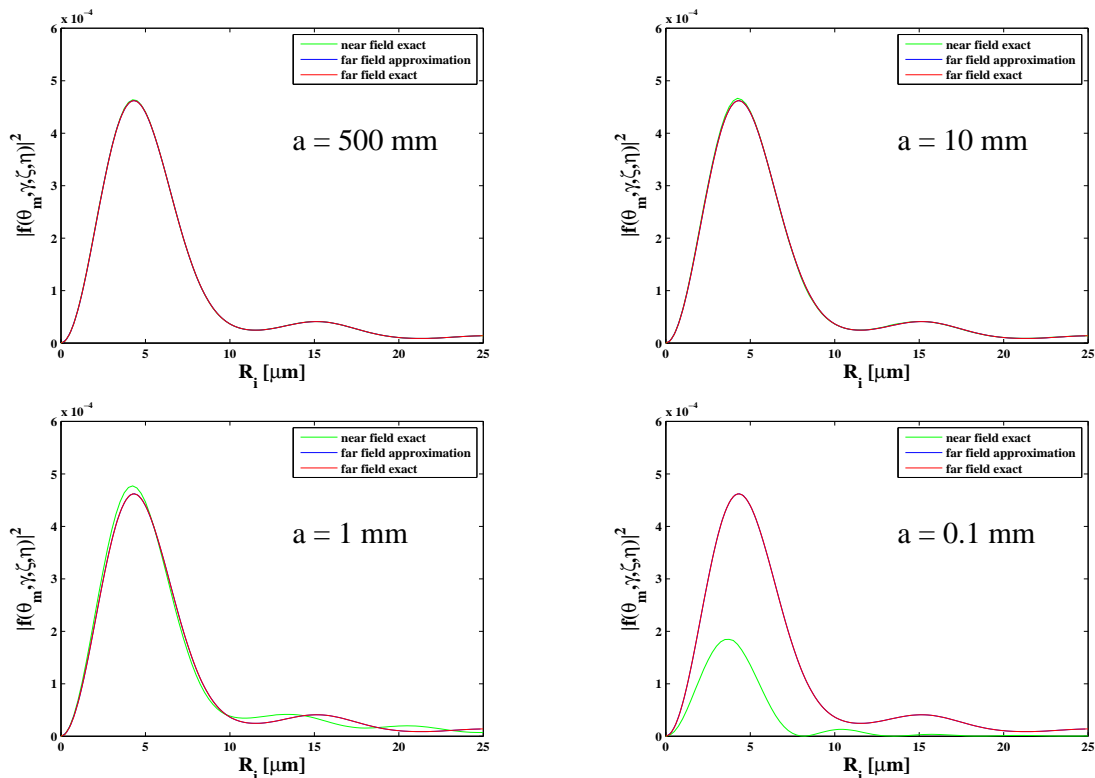
Figure 6: OTR images with near field calculation Eq.(16), far field calculation Eq.(23) and approximative far field calculation Eq.(25) for a 20 GeV electron beam, a 1:1 optical imaging system and an observation wavelength $\lambda = 500$ nm. The lens aperture θ_m was kept constant assuming a lens diameter of $\oslash$ 50.8 mm for the maximum distance $a = 0.5$ m.

3.3 OTR Imaging in the Far Field: Influence of the optical System

So far only the evolution of the wave front in view of the pre–wave zone effect was under investigation. While inspecting Eqn.(23), (25) and (26) which are the basis of the far field calculation it can be seen that the SPF strongly depends on the lens aperture θ_m. In this subsection therefore the influence of the lens diameter is studied more in detail.

Fig.7 shows a comparison of SPFs for various lens diameters which are commercially available. The calculations have been performed assuming Eq.(23). From this it is clear to see that the resolution of the OTR monitor is strongly determined by the lens diameter resp. the numerical aperture of the optical system, in close analogy to imaging in classical optics.

In the following an estimate for the monitor resolution will be given. In accordance with the diffraction limited resolution of a point source in classical optics the resolution is defined as the first minimum of the SPF (apart from the central minimum). Due to the fact that for the parameters presented here the SPF is well described by the analytical approximation Eq.(25), it is sufficient to inspect this equation more in detail which has the general form $K_1(x) - 1/x\, J_0(x)$. While $K_1(x)$ is continuously decaying, $J_0(x)$ shows oscillatory behavior. Due to the fact that both functions are subtracted from each other, the first minimum apart from the central one is determined by the second maximum of $J_0(x)$ which is located at $x_0 = 7.0160$, i.e. the resolution is defined by

$$\zeta_0\, \theta_m = 7.0160 \ .$$

Rewriting this condition in physical variables rather than in dimensionless ones the result for the monitor resolution reads

$$R_{i0} \approx 1.12\, \frac{M\lambda}{\theta_m} \ , \tag{30}$$

i.e. the resolution of an OTR monitor is fully determined by the magnification M, the wavelength of observation λ and the acceptance angle θ_m of the optical system. With the parameters of Fig.7 and according to Eq.(30) the resolutions are estimated to be 5.6 μm ($\oslash$ 100 mm), 11.0 μm ($\oslash$ 50.8

mm), 22.0 μm ($\oslash$ 25.4 mm), and 44.8 μm ($\oslash$ 12.5 mm) which is in very good agreement with the calculations shown in Fig.7.

Furthermore keeping in mind that the diffraction limited resolution of a point source in classical optics is defined via the radius of the Airy disk which is $R_{Airy} \approx 0.61 \frac{M\lambda}{\theta_m}$, it follows that the resolution of an OTR monitor is about two times larger than the one for a point source.
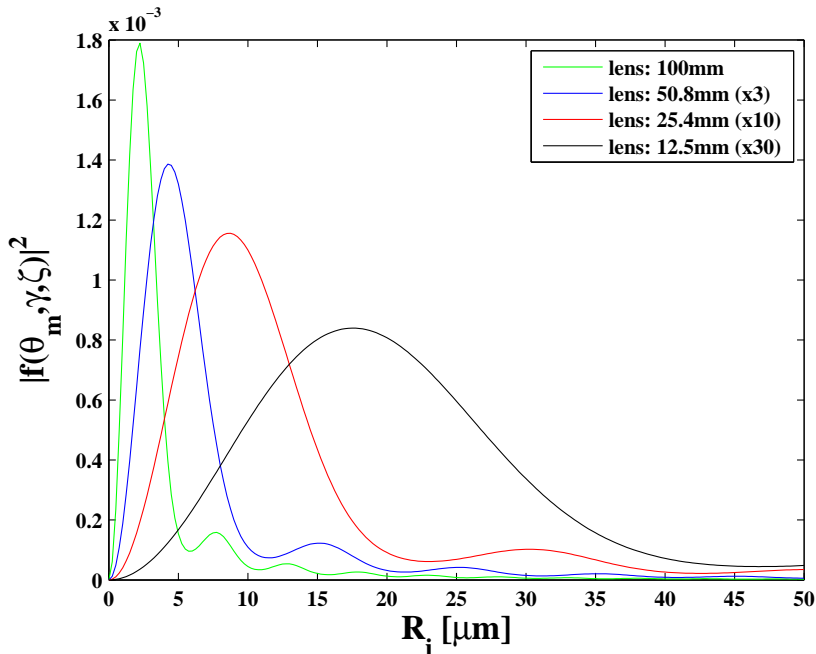

Figure 7: Influence of the optical system acceptance angle on the OTR images, assuming far field conditions according to Eq.(23). Parameters of calculation: 20 GeV electron beam, 1:1 magnification ($a = b = 0.5$ m), and an observation wavelength $\lambda = 500$ nm. The lens apertures were chosen such that they correspond to standard commercially available achromatic lenses. For better visibility the different curves are scaled in amplitude as indicated in the legend.

3.3.1 Improvement of Resolution

Two important aspects can be directly deduced from Eq.(30). Firstly the lens aperture should be chosen reasonable large. In the same manner there should be additionally no further obstacles like the extraction window of the vacuum chamber which reduces the free aperture of the optical system, because it affects the monitor resolution in the same way. Secondly the wavelength of observation should be chosen as small as possible, keeping in mind the detector sensitivity (at FLASH for example digital CCD cameras, model Basler A301f are used [7] which have a sensitivity from about $\lambda = 400$ nm up to 1000 nm with the maximum at 500 nm [29]). If in a single shot image the OTR intensity is sufficient enough it is recommended to use narrow band optical filters, preventing the resolution to be smeared out. The use of bandpass filters has the additional advantage that chromatic errors due to the optical system can be minimized in advance. These chromatic errors can also be reduced by the use of achromatic or even apochromatic lenses, but an achromat is corrected only for two wavelengths (F line at 486.1 nm and C line at 656.3 nm in spectroscopic notation) and an apochromat for three (F, C and d line at 587.6 nm), consequently a residual spectrum remains [30].

Apart from these considerations an other possibility to improve the OTR monitor resolution which was discussed already in Refs.[14, 15] is to introduce a mask just in front of the lens. Due to the fact that the expression of a diffraction limited resolution is nothing else than another formulation of the uncertainty principle, the effect of the mask can be interpreted as increasing the uncertainty in the momentum ($\rightarrow$ mask out small emission angles) for to reduce the uncertainty in the position ($\rightarrow$ improve resolution) - or in other words, while blocking the photons emitted under small angles the intensity in the tails of the SPF is reduced. Mathematically the effect of the mask is described

starting from Eq.(23)

$$f(\theta_m, \gamma, \zeta) = \int\limits_{\theta_b}^{\theta_m} \mathrm{d}\theta \; \frac{\theta^2}{\theta^2 + 1/\gamma^2} \; \mathrm{J}_1(\zeta\theta). \tag{31}$$

Similar to the derivation of Eqn.(25) resp. (26) it is assumed that $\theta_m, \theta_b \gg 1/\gamma$, which results in the following expression:

$$\begin{aligned}
f(\theta_b, \theta_m, \zeta) &= \int\limits_{\theta_b}^{\infty} \mathrm{d}\theta \; \mathrm{J}_1(\zeta\theta) - \int\limits_{\theta_m}^{\infty} \mathrm{d}\theta \; \mathrm{J}_1(\zeta\theta) \;, \\
&= \zeta^{-1} \left[\mathrm{J}_0(\zeta\theta_b) - \mathrm{J}_0(\zeta\theta_m) \right].
\end{aligned} \tag{32}$$

In Fig.8 the influence of the mask on the SPF in the image plane is calculated for typical parameters under consideration for the XFEL. As can be seen the effect of the mask is to suppress the oscillatory structure of the SPF, resulting in a resolution improvement. At the other hand the usage of a mask leads to an additional decrease of the intensity.
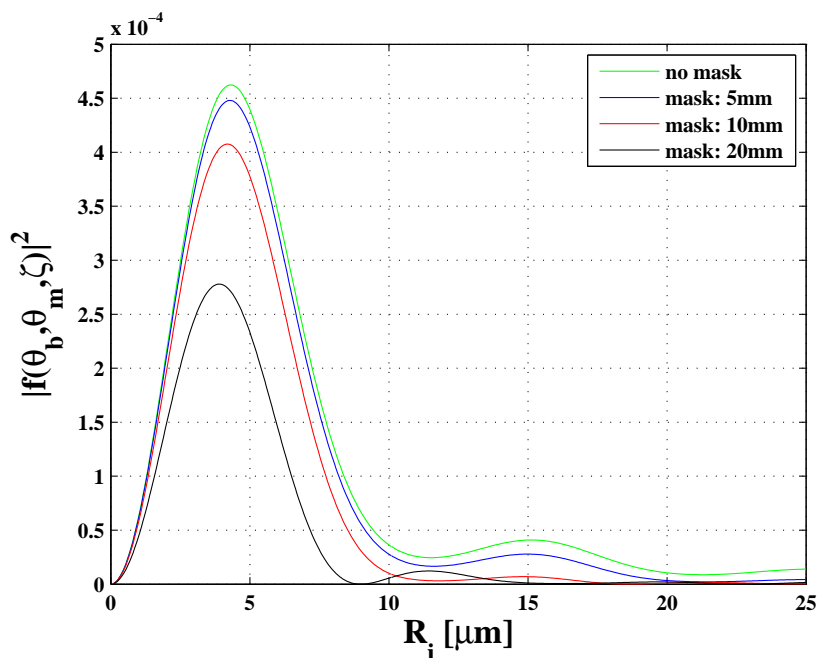

Figure 8: Influence of the mask in front of the lens on the SPF according to Eq.(32) for various mask diameters, assuming far field conditions and $\theta_m, \theta_b \gg 1/\gamma$. Parameters of calculation: 20 GeV electron beam, 1:1 magnification ($a = b = 0.5$ m), wavelength $\lambda = 500$ nm, and lens diameter $\oslash$ 50.8 mm.

In the following a short estimate for an optimum mask size will be given in the approximation of the analytical expression Eq.(32). Inspecting the form of this equation, the SPF is determined by the difference of two Bessel functions J_0, while each of these functions exhibits an oscillatory behavior. The idea is to cancel out the oscillations of the first Bessel function with the ones of the second function in the outer tail. To a very good approximation this can be achieved if the first zero of the Bessel function $\mathrm{J}_0(\zeta\theta_b)$ coincides with the third zero of the function $\mathrm{J}_0(\zeta\theta_m)$, i.e. for the condition

$$\zeta\theta_{b0} = 2.4048 \qquad \text{and} \qquad \zeta\theta_m = 8.6537 \;.$$

From these conditions it follows directly that the diameter of the mask is related to the diameter of the lens by

$$\oslash_b = 0.2779 \; \oslash_m \;, \tag{33}$$

i.e. the optimum mask size is independent from beam energy and observation wavelength in the approximation under consideration and is simply determined by the lens diameter. Fig.9 shows
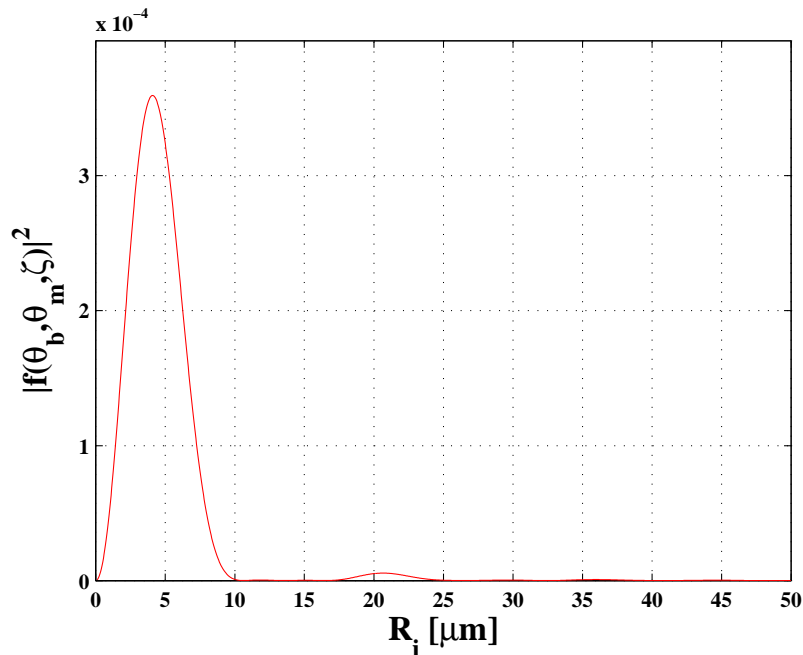
Figure 9: Calculation of the SPF for a mask with optimized size according to Eq.(33). Parameters of calculation: 20 GeV electron beam, 1:1 magnification ($a = b = 0.5$ m), wavelength $\lambda = 500$ nm, lens diameter $\oslash$ 50.8 mm, and mask diameter 14.12 mm.

a calculation of the SPF for an optimized mask size according to Eq.(33). As can be seen the oscillatory structure of the SPF is canceled out over a wide range in the image plane, render it possible to resolve even the outer tails of the beam profile.

In the calculations presented in this section it was assumed all the time that the mask is perfectly centered with respect to the optical axis. If it is not the case this will lead to a distortion of the SPF. However, this effect is not point of investigation in this note and will be investigated at a later time.

3.3.2 OTR Imaging with misaligned optical System

Up to know it was assumed that the optical system is perfectly aligned, i.e. that condition Eq.(8) holds. In this case the additional phase factor (written in polar coordinates, i.e. $x_l = R_l \cos\varphi_l$ and $y_l = R_l \sin\varphi_l$)

$$\exp\left(-i\frac{kR_l^2}{2}\left(1/f - 1/a - 1/b\right)\right)$$

appearing in Eq.(7) cancels out, just simplifying the calculation. In the following a slightly misaligned optical system is considered and the impact on the resolution is studied. To do so a perfectly aligned system with object distance a_0 and image distance b_0 is considered for which the condition for imaging is still valid, i.e.

$$\frac{1}{f} - \frac{1}{a_0} - \frac{1}{b_0} = 0 \ .$$

In a slightly misaligned system with $a = a_0 + \Delta a$ resp. $b = b_0 + \Delta b$ the condition reads

$$\frac{1}{f} - \frac{1}{a_0}\frac{1}{1 + \Delta a/a_0} - \frac{1}{b_0}\frac{1}{1 + \Delta b/b_0} \ .$$

For small alignment errors ($\Delta a, b \ll a_0, b_0$) it is

$$\begin{aligned}
\frac{1}{f} - \frac{1}{a_0}\left(1 - \frac{\Delta a}{a_0}\right) - \frac{1}{b_0}\left(1 - \frac{\Delta b}{b_0}\right) &= \frac{1}{f} - \frac{1}{a_0} - \frac{1}{b_0} + \frac{\Delta a}{a_0^2} + \frac{\Delta b}{b_0^2} \\
&= \frac{\Delta a}{a_0^2} + \frac{\Delta b}{b_0^2} \ ,
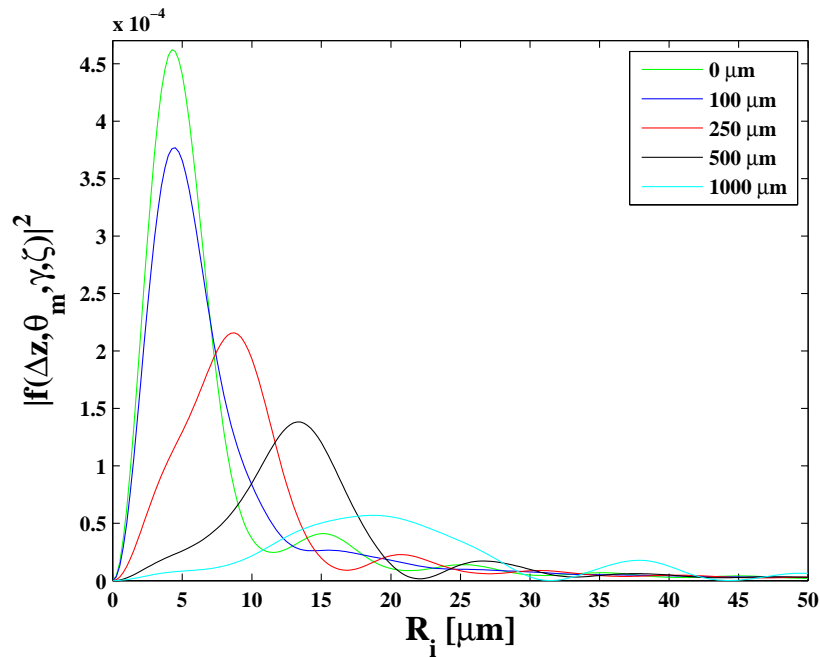\end{aligned} \tag{34}$$

Figure 10: Calculation of the SPF taking into account a misaligned optical systems for various misalignments Δz (with z object resp. image distance). Parameters of calculation: 20 GeV electron beam, 1:1 magnification ($a = b = 0.5$ m), wavelength $\lambda = 500$ nm, and lens diameter $\oslash$ 50.8 mm. The impact on the SPF is the same for a misalignment $+\Delta z$ or $-\Delta z$.

and the additional phase factor is given by

$$\exp\left(-i\frac{kR_l^2}{2}\left[\frac{\Delta a}{a_0^2} + \frac{\Delta b}{b_0^2}\right]\right) = \exp\left(-i\frac{k}{2}\theta^2\left[\Delta a + \frac{\Delta b}{M^2}\right]\right) . \tag{35}$$
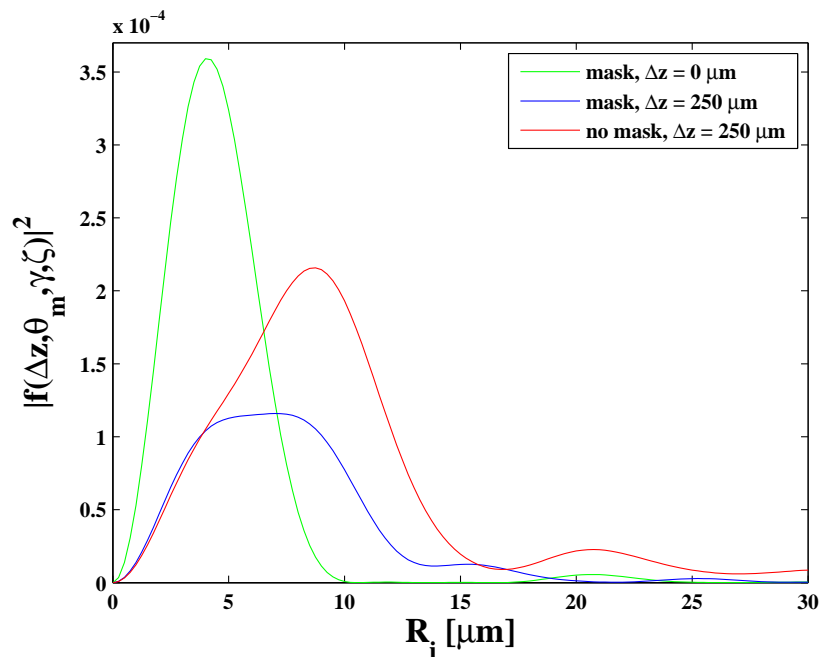

Figure 11: Calculation of the SPF for an aligned and a misaligned optical system, taking into account the influence of the mask discussed in the previous section. Parameters of calculation: 20 GeV electron beam, 1:1 magnification ($a = b = 0.5$ m), wavelength $\lambda = 500$ nm, and lens diameter $\oslash$ 50.8 mm. For the mask the optimized diameter of 14.12 mm was assumed.

The integration over the lens aperture was carried out at the end in the derivation of far field OTR, therefore the additional phase factor is simply attached to the result Eq.(23):

$$f(\Delta z, \theta_m, \gamma, \zeta) = \int\limits_0^{\theta_m} d\theta \; \frac{\theta^2}{\theta^2 + 1/\gamma^2} \; J_1(\zeta\theta) \; e^{-i\frac{k}{2}\theta^2 (\Delta a + \frac{\Delta b}{M^2})} \tag{36}$$

with Δz the misalignment either in image or in object distance. Eq.(36) is the basis for the discussion of the misalignment of the optical system presented in the following.

In Fig.10 calculations of the SPF for different misalignments are shown with typical parameters for the XFEL. The magnification was chosen as $M = 1$, i.e. a misalignment in the object distance has the same impact on the SPF than a misalignment in the image distance according to Eq.(36). As can be seen, due to a misaligned optical system either in object or in image plane, the SPF and consequently the resolution is strongly affected. For the same set of parameters but a lens with larger diameter the difference between perturbed and unperturbed SPF is even more pronounced because of the θ^2 dependence of the phase term in Eq.(36). However, the resolution (defined as the first minimum of the SPF apart of the central one) remains still better than for smaller lens diameters.

Assuming somehow arbitrary that the broadening of the SPF should not exceed more than 50%, for the calculations shown in Fig.10 the consequence is that the absolute accuracy in the alignment of the optical system should be better than 250 μm (increase from $\sim$ 10 μm to 15 μm). The future XFEL OTR monitors should be provided therefore with accurate alignment stages for lens and/or detector.

In the previous section the use of a mask was discussed in order to improve the monitor resolution by suppressing the oscillatory behavior of the SPF in the tails. In Fig.11 a comparison is shown for typical XFEL parameters and the maximum allowed misalignment of 250 μm, taking into account the influence of the mask. The calculations were performed for the optimized mask diameter of 14.12 mm (for a lens diameter of 50.8 mm). As can be seen, by means of the mask it is again possible to slightly improve the monitor resolution.
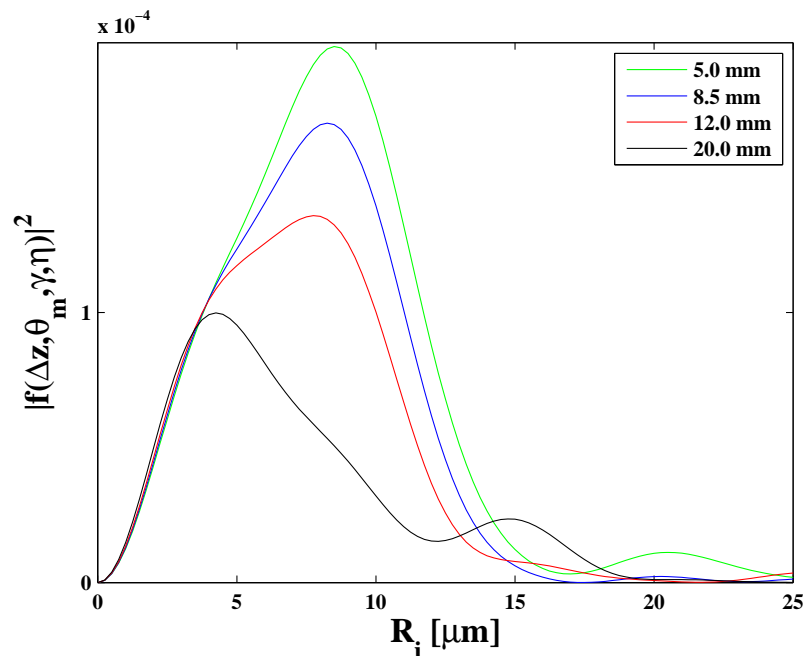

Figure 12: Calculation of the SPF for a misaligned optical system with $\Delta z = 250$ μm with the mask diameter as parameter. Parameters of calculation: 20 GeV electron beam, 1:1 magnification ($a = b = 0.5$ m), wavelength $\lambda = 500$ nm, and lens diameter $\oslash$ 50.8 mm.

In Fig.12 SPFs calculated for the same parameters are shown with the mask diameter as parameter. It follows that the most suitable mask diameter now is about 8.5 mm, i.e. slightly smaller than
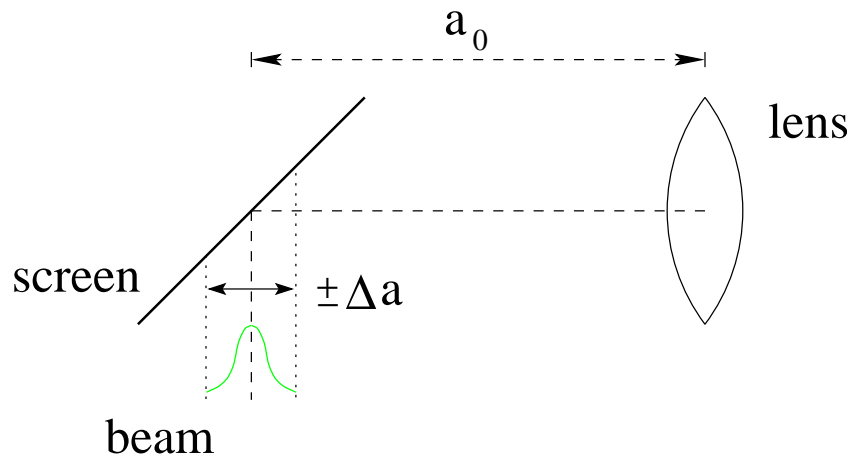
Figure 13: Beam imaging with backward OTR from an inclined target. Due to the screen inclination different parts from the beam are located at different object distances.

without taking into account the optical misalignment. If for example $\Delta z = 100\ \mu$m is assumed, the best condition is achieved with a mask diameter of about 12 mm. From the calculations presented here it can be concluded that as larger a misalignment in the optical system, as smaller the mask diameter in order to suppress the oscillatory structure in the tails of the SPF.

So far it was assumed that the longitudinal shift Δz is due to a misalignment of the object resp. image plane. At the other hand keeping in mind that conventional OTR diagnostics is based on backward emitted radiation from an inclined target with respect to the beam axis, it follows directly that an extended object like a beam profile will not be exactly located in the object plane of the lens because of the inclination. For better illustration the situation is sketched in Fig.13. The case is considered that the location of the beam center on the screen coincides with the object distance a_0. Due to the finite extensions of the object (beam) the tails appears at different locations, slightly shifted away from a_0 by an amount $\pm\Delta a$. This longitudinal shift causes a blurring of the image in the outer parts, i.e. the tails of the beam are imaged with degraded resolution in comparison to the center. The situation becomes worse for large beam profiles and for large screen inclination angles. Assuming a somehow idealistic rectangular beam profile with size $\sigma = \pm\ 250\ \mu$m and a screen inclination of $\Psi = 45°$ as shown in Fig.13, then the difference in the object distance is $\Delta a = \pm\sigma\tan\Phi = \pm\ 250\ \mu$m. If a screen inclination angle of $\Psi = 20°$ is chosen, the shift in the object distance reduces to $\Delta a = \pm\ 91\ \mu$m which improves the situation. For the design of the XFEL OTR monitors other geometries than the conventional 90° backward observation ones should at least be considered.
Alternatively in order to maintain the focus over the whole target screen an other option to be considered is to rotate the camera in Scheimpflug condition. Such a scheme was already realized in the FNAL proton and antiproton OTR monitors [31].

4   Preliminary Design Considerations

In this section some basic design considerations for the layout of an OTR monitor optical system will be outlined, assuming a perfect aligned system without central mask for resolution improvement. Starting point is the estimate for the OTR resolution including the optical system Eq.(30), based on the first minimum of the SPF. However, the expression derived there describes the SPF in the image plane. For a direct comparison of the resolution with the beam size in the source plane it is suitable to disregard the magnification M of the optics, and the OTR resolution reads

$$\sigma_{OTR} = 2.24\,\frac{a\lambda}{\oslash_l} \tag{37}$$

with $\oslash_l$ the lens diameter, keeping in mind the definition Eq.(13) of the collection angle θ_m.

The discussion of the design of an optical system in terms of the object distance a is not practicable, it is more convenient to have in mind the total optical path length $L = a + b$ (because of space

requirements), the magnification $M = b/a$ (because of the camera field of view), and the focal length f of the lens. By means of these relations, Eq.(8) can simply be converted in the following applicable forms

$$
\begin{aligned}
f &= \frac{M}{(M+1)^2} L \\
a &= (1 + 1/M)f = \frac{1}{1+M} L \\
b &= (1 + M)f = \frac{M}{1+M} L.
\end{aligned}
$$

Inserting a in Eq.(37) results in an equation for the OTR resolution, taking into account the appropriate parameters for the monitor design:

$$
\sigma_{OTR} = 2.24 \, \frac{\lambda}{\oslash_l} \frac{L}{1+M} \ . \tag{38}
$$

According to this equation it is clear that for a high resolution OTR monitor design the use of a short distance L optical system with high magnification M and large lens diameter $\oslash_l$ has to be aimed, and the observation wavelength λ should be as small as possible.

For an estimate of the OTR monitor resolution the pixel size Δ_p of the CCD camera has additionally to be taken into account. Keeping in mind that Δ_p is related to the image plane, for a direct comparison with the beam size it has to be re–projected in the source plane, and the resolution contribution is

$$
\sigma_{CCD} = \Delta_p/M \ . \tag{39}
$$

The total resolution is achieved by quadratical summation of both contributions

$$
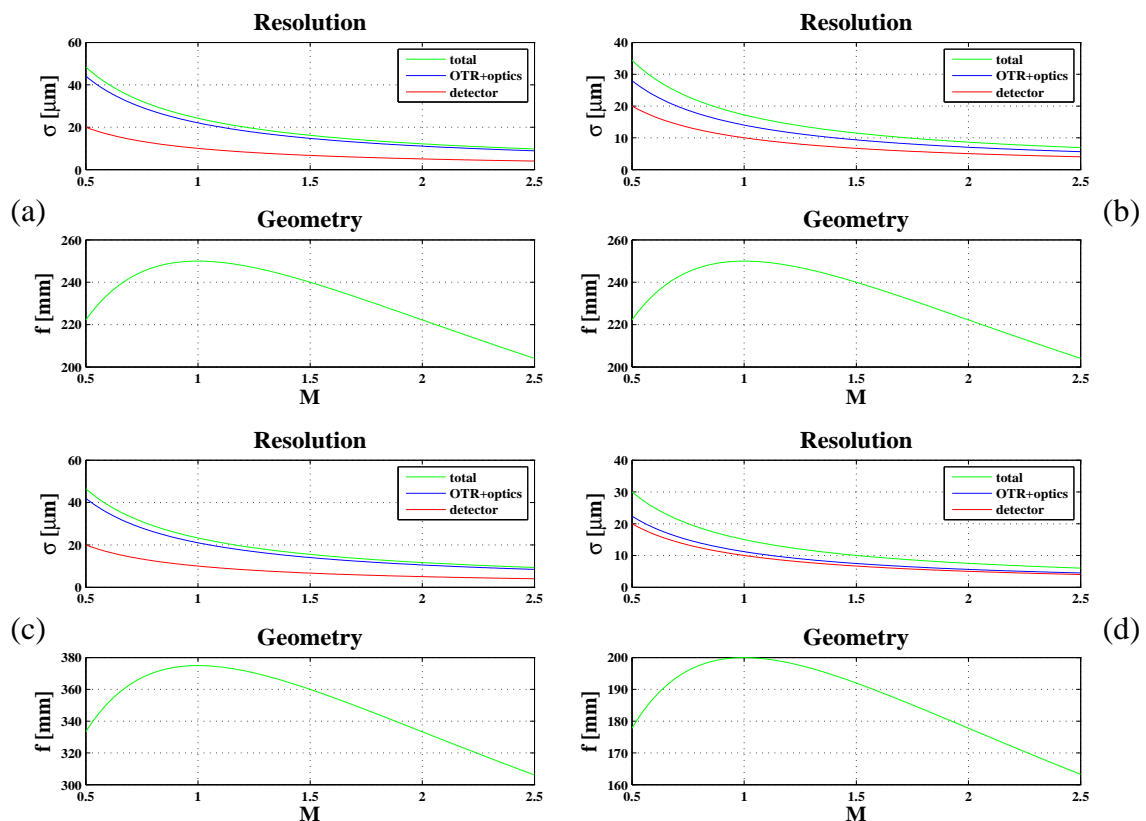\sigma = \sqrt{\sigma_{CCD}^2 + \sigma_{OTR}^2} \ . \tag{40}
$$

Figure 14: Calculated resolutions and focal lengths for an OTR monitor as function of the magnification. The parameters of calculation are $\lambda = 500$ nm, pixel size $\Delta_p = 10$ μm, and (a) $\oslash_l$ 50.8 mm, L = 1 m, (b) $\oslash_l$ 80 mm, L = 1 m, (c) $\oslash_l$ 80 mm, L = 1.5 m, (d) $\oslash_l$ 80 mm, L = 0.8 m.

Fig.14 shows calculations of the monitor resolution as function of the magnification M together with the functional dependency of the focal length f according to Eqs.(38)–(40). With the requirement of a total resolution $\sigma \approx 10$ μm and the calculations presented, it can be concluded that this demand will only be fulfilled with a magnification $M > 1$. Then again, a large magnification and good resolution typically requires the use of large diameter and short focus lenses, which are not easy to find commercially. However, achromatic lenses with $\oslash_l$ 80 mm and $f = 310$ resp. 160 mm exist (see e.g. [32]), and with a proper choice of the parameters the resolution can be achieved.

At the one hand a magnification $M > 1$ helps to reduce the alignment requirements for the image distance as can be seen from Eq.(36). At the other hand it should be pointed out that the use of a magnification $M > 1$ restricts the field of view of the CCD camera, and in some cases it might be possible that the requisite field of view restricts the monitor resolution. One way to balance both effects is to reduce the optical path length L. Fig.15 shows the result of such optimization, assuming a commercially available achromatic lens with $\oslash_l$ 80 mm, $f = 160$ mm (see above) and observation at $\lambda = 500$ nm together with an optical path length of $L = 0.65$ m. As can be seen the requirements are nearly fulfilled at a magnification of about $M \approx 1.25$.
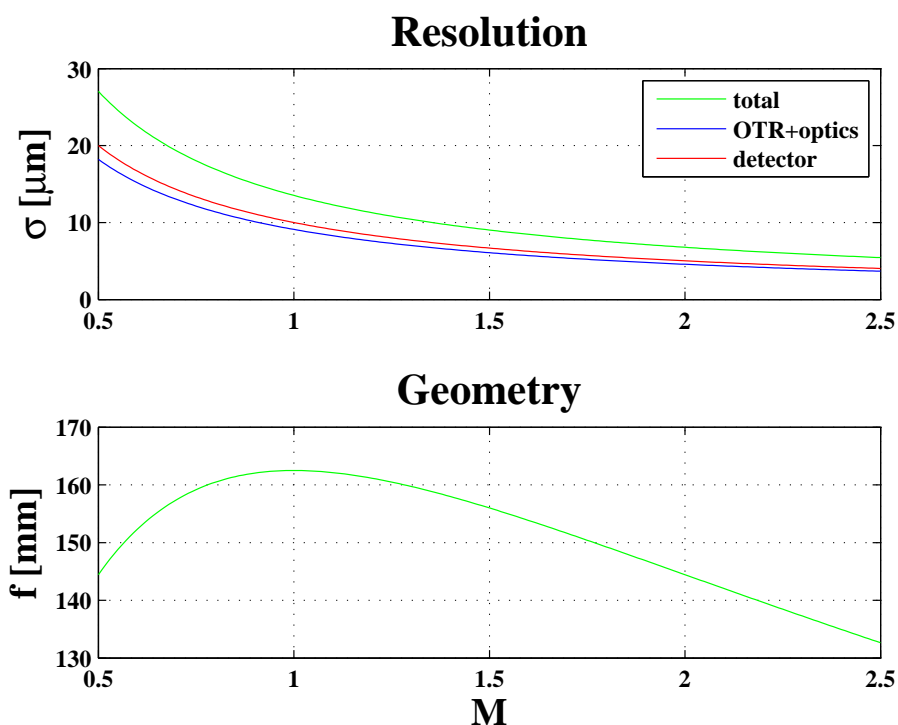

Figure 15: Calculated OTR monitor resolutions and focal lengths as function of the magnification for $\lambda = 500$ nm, pixel size $\Delta_p = 10$ μm, $\oslash_l$ 80 mm, and L = 0.65 m. At a magnification of about $M \approx 1.25$ the total resolution amounts $\sigma \approx 10$ μm, and the focal length is $f = 160$ mm which allows the use of a commercially available achromatic lens [32].

To be more precise according to Eqs.(38) and (40), magnification and optical path length of the system can be calculated for given lens parameters $(f, \oslash_l)$, detector pixel size Δ_p and required resolution σ:

$$M_{opt} = \frac{\xi^2 + \sqrt{\sigma^2 \xi^2 + \sigma^2 \Delta_p^2 - \xi^2 \Delta_p^2}}{\sigma^2 - \xi^2} \tag{41}$$

$$\text{with} \quad \xi = 2.24 \frac{\lambda f}{\oslash_l} \, ,$$

$$L_{opt} = \frac{(M_{opt} + 1)^2}{M_{opt}} f \, . \tag{42}$$

With the parameters mentioned above this would result in a magnification of $M_{opt} = 1.106$ and a length of $L_{opt} = 0.642$ m. For these values the distance between source and lens would amount only $a \approx 0.30$ m, i.e. the lens would be situated very close to the screen.

According to the definition of the magnification, M represents a positive value. Taking into account this constraint it follows directly from Eq.(41) that the following condition must hold:

$$\sigma > \xi = 2.24 \frac{\lambda f}{\oslash_l} \ . \tag{43}$$

Eq.(43) relates the lens parameters ($\oslash_l$, f) and the wavelength of observation λ directly with the minimum achievable resolution, i.e. if this condition is not fulfilled the optical system will provide no imaging. If the so called lens factor ξ approaches the resolution the magnification increases drastically, cf. also Fig.16.
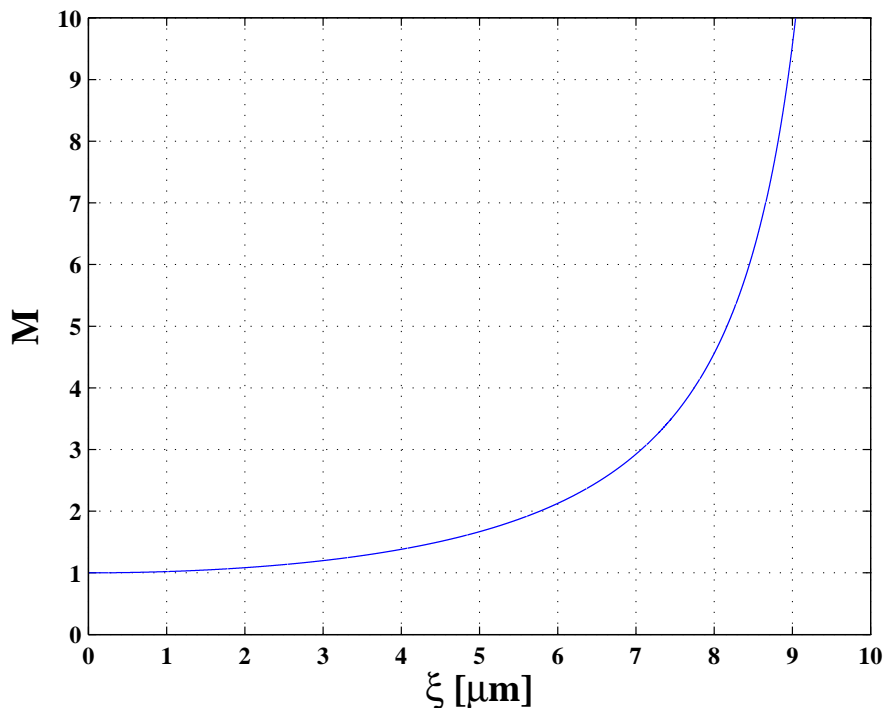

Figure 16: Magnification of the optical system as function of the lens factor ξ according to Eq.(41), assuming a resolution of $\sigma = 10$ μm and a CCD pixel size of the same value.

As smaller the lens factor in comparison with the monitor resolution, as smaller the required magnification of the optical system. It is also of interest to inspect Eq.(41) in the limit of small lens parameter, i.e. for

$$\lim_{\xi \to 0} M_{opt} = \frac{\Delta_p}{\sigma} \ . \tag{44}$$

As can be seen from this equation together with Fig.16 the minimum magnification of the optical system is defined by the pixel size Δ_p and the resolution σ. This result is not surprising because the limit $\xi \to 0$ represents nothing else than the statement that the OTR resolution Eq.(38) is negligible in comparison to the the CCD resolution Eq.(39), and therefore the total resolution Eq.(40) is determined by the latter contribution.

For illustration in the following two example calculations are performed for an optimization of the OTR monitor resolution (disregarding from influences like lens errors, alignment tolerances ...). For a high resolution monitor with a required resolution of $\sigma = 1$ μm, a CCD camera with pixel size $\Delta_p = 5$ μm, and assuming a lens with $f = 40$ mm, $\oslash_l$ 50.8 mm, in case of observation at $\lambda = 500$ nm (i.e. $\xi = 0.882$) the monitor parameters are $M_{opt} = 14.82$ and $L_{opt} = 0.845$ m. In case of observation at $\lambda = 400$ nm (i.e. $\xi = 0.706$) both parameters are reduced, resulting in $M_{opt} = 8.18$ and $L_{opt} = 0.41$ m.

From the estimations presented so far, the following conclusions can be drawn for a high resolution OTR monitor: (i) the lens requires a large collection angle and a short focal length, and additionally (ii) the wavelength of observation should be as small as possible. Both statements are consequences

from Eq.(43). According to Eq.(42), due to the small focal length (iii) the overall optical path length will be small. To keep the lens parameters in a reasonable range is easier to fulfill if the lens factor ξ is not to far away from σ, i.e. typically (iv) a large optical magnification is necessary. Finally (v) the detector pixel size should be as small as possible.

These are in principle the aspects on which the design of the high resolution OTR beam profile monitor presented in Ref.[18] is based. Nevertheless, from the practical operational point of view the drawback of such "short distance L–geometry" is that the camera would have a direct view to the screen because the small length L would not allow to use a deflecting mirror for detector protection.

5 Summary

In this note the imaging of OTR was considered from a theoretical point of view with special emphasis on the design of a transverse beam size monitor for the XFEL. The principle of imaging was explained in the frame of conventional scalar diffraction theory and basic formulas to calculate the intensity distribution of a single electron in the image plane (single particle function SPF) were derived following Refs.[1, 2].

- Based on the theory it was demonstrated that the influence of the pre–wave zone effect is negligible in the imaging process, although the angular distribution of the radiation at the location of the lens is strongly affected.

- Detailed resolution studies were performed and it was shown that the OTR resolution is about two times larger than the diffraction limited one of a point source in classical optics. The resolution is mainly determined by the wavelength of observation and the collection angle of the optical system. For the XFEL monitor design the use of narrow–band short–wavelength radiation and a large angle optical collection system should therefore be considered, carefully avoiding any additional restrictions of the free aperture.

- The monitor performance can be increased by use of a mask located in front of the lens which blocks the photons emitted under small angles with respect to the beam axis. With help of this mask the monitor resolution can be improved and the oscillatory structure of the SPF can be suppressed. A simple estimate for an optimized mask diameter was derived which is only a function of the lens aperture.
  Nevertheless the use of such mask has to be assessed carefully, keeping in mind the effort for manufacturing and alignment of this system and additionally taking into account the spatial resolution of the CCD detector. With help of the formulas derived in this note for the FLASH OTR monitors for example, the resolution is calculated to be about 10 μm (assuming 1:1 magnification at 500 nm). By usage of a mask the resolution could be reduced by 1–2 μm, but due to the finite pixel size (9.9 μm × 9.9 μm) of the CCD used in this monitor [7] this improvement will not be resolved.

- The influence of a misaligned optical system was studied and it was shown that the monitor resolution strongly depends on the quality of alignment. Therefore in the monitor design accurate alignment stages should be provided for lens and/or detector.

- Anyhow, due to the inclination of the target screen a residual image blurring remains. For reduction of this image deterioration it should be considered whether a screen geometry with reduced inclination angle with respect to the beam axis could be used.

- Finally design considerations for the optical system were outlined. With the help of Eqs.(41), (42) and (43) it is possible to fix the general OTR monitor parameters based on simple principles, before more elaborate optical design software as e.g. ZEMAX [33] is applied.
  It was shown that a high resolution OTR monitor design requires the use of a short distance L optical system with high magnification M and large lens diameter $\oslash_l$, and additionally the observation wavelength λ should be chosen small.
  However, the high magnification might be in contradiction to the required field of view of the optical system. In order to balance these effects it is possible to reduce the overall length L of the system with the drawback that the sensitive CCD camera has direct view to the

OTR screen, which might cause damage of the camera due to a higher radiation background. Therefore such a solution has to be studied carefully by additional background simulations.

6 Appendix

In this appendix the basic representations for the fields of an ultra relativistic particle moving with constant velocity will be deduced as they are used as input for the investigation of optical transition radiation (OTR) resp. optical diffraction radiation (ODR) [1, 2]. Starting point for the derivation are the Maxwell equations which are applied in cgs units:

$$
\begin{aligned}
\vec{\nabla} \cdot \vec{D}(\vec{r}, t) &= 4\pi \, \rho(\vec{r}, t) \\
\vec{\nabla} \times \vec{H}(\vec{r}, t) &= \frac{4\pi}{c} \, \vec{J}(\vec{r}, t) + \frac{1}{c} \, \dot{\vec{D}}(\vec{r}, t) \\
\vec{\nabla} \cdot \vec{B}(\vec{r}, t) &= 0 \\
\vec{\nabla} \times \vec{E}(\vec{r}, t) &= -\frac{1}{c} \, \dot{\vec{B}}(\vec{r}, t)
\end{aligned}
\tag{45}
$$

with $\vec{D} = \vec{E}$ and $\vec{H} = \vec{B}$ in vacuum, i.e. $\varepsilon = \mu = 1$. By introducing the potentials

$$
\begin{aligned}
\vec{B}(\vec{r}, t) &= \vec{\nabla} \times \vec{A}(\vec{r}, t) \\
\vec{E}(\vec{r}, t) &= -\vec{\nabla}\varphi(\vec{r}, t) - \frac{1}{c} \, \dot{\vec{A}}(\vec{r}, t)
\end{aligned}
\tag{46}
$$

and taking into account the Lorentz gauge

$$
\vec{\nabla} \cdot \vec{A} + \frac{1}{c} \frac{\partial \varphi}{\partial t} = 0
$$

the wave equations for the potentials are deduced

$$
\begin{aligned}
\vec{\nabla}^2 \vec{A}(\vec{r}, t) - \frac{1}{c^2} \frac{\partial^2}{\partial t^2} \vec{A}(\vec{r}, t) &= -\frac{4\pi}{c} \, \vec{J}(\vec{r}, t) \\
\vec{\nabla}^2 \varphi(\vec{r}, t) - \frac{1}{c^2} \frac{\partial^2}{\partial t^2} \varphi(\vec{r}, t) &= -4\pi \, \rho(\vec{r}, t)
\end{aligned}
$$

which have to be solved. Due to practical reasons the solution of these differential equations is performed in the frequency domain with the Fourier transform taken in the following form

$$
\begin{aligned}
\vec{A}(\vec{r}, t) &= \int \mathrm{d}\omega \int \mathrm{d}^3\vec{k} \, \vec{A}(\vec{k}, \omega) e^{i(\vec{k}\cdot\vec{r} - \omega t)} \\
\vec{A}(\vec{k}, \omega) &= \frac{1}{(2\pi)^4} \int \mathrm{d}t \int \mathrm{d}^3\vec{r} \, \vec{A}(\vec{r}, t) e^{-i(\vec{k}\cdot\vec{r} - \omega t)},
\end{aligned}
$$

and in analogous way for the scalar potential $\varphi(\vec{r}, t)$.

$$
\begin{aligned}
(\vec{k}^2 - \frac{\omega^2}{c^2}) \, \vec{A}(\vec{k}, \omega) &= \frac{4\pi}{c} \, \vec{J}(\vec{k}, \omega) = \frac{4\pi}{c} \frac{1}{(2\pi)^4} \int \mathrm{d}t \int \mathrm{d}^3\vec{r} \, \vec{J}(\vec{r}, t) e^{-i(\vec{k}\cdot\vec{r} - \omega t)} \\
(\vec{k}^2 - \frac{\omega^2}{c^2}) \, \varphi(\vec{k}, \omega) &= 4\pi \, \rho(\vec{k}, \omega) = 4\pi \frac{1}{(2\pi)^4} \int \mathrm{d}t \int \mathrm{d}^3\vec{r} \, \rho(\vec{r}, t) e^{-i(\vec{k}\cdot\vec{r} - \omega t)}
\end{aligned}
$$

Considering a point-like source with charge e which moves with constant velocity $\vec{v}$:

$$
\begin{aligned}
\vec{J}(\vec{r}, t) &= e \, \vec{v} \, \delta(\vec{r} - \vec{r}(t)) \\
\rho(\vec{r}, t) &= e \, \delta(\vec{r} - \vec{r}(t)).
\end{aligned}
$$

In this case the integration in the space domain can be carried out directly, resulting in

$$
\vec{A}(\vec{k}, \omega) = \frac{e\vec{v}}{4\pi^3 c} \, (k^2 - \omega^2/c^2)^{-1} \int\limits_{-\infty}^{+\infty} \mathrm{d}t \, e^{i(\omega t - \vec{k}\cdot\vec{r}(t))}
$$

$$
\varphi(\vec{k}, \omega) = \frac{e}{4\pi^3} \, (k^2 - \omega^2/c^2)^{-1} \int\limits_{-\infty}^{+\infty} \mathrm{d}t \, e^{i(\omega t - \vec{k}\cdot\vec{r}(t))}.
$$

With the replacement $\vec{r}(t) = \vec{v}t$, the integration in the time domain can be performed

$$\int\limits_{-\infty}^{+\infty} dt \, e^{i(\omega t - \vec{k} \cdot \vec{r}(t))} = \int\limits_{-\infty}^{+\infty} dt \, e^{i(\omega - \vec{k} \cdot \vec{v})t} = 2\pi \, \delta(\omega - \vec{k} \cdot \vec{v})$$

and the solution for the potentials in the frequency/wave number domain is obtained:

$$\vec{A}(\vec{k}, \omega) = \frac{e}{2\pi^2 c} \vec{v} \frac{\delta(\omega - \vec{k} \cdot \vec{v})}{k^2 - \omega^2/c^2}$$

$$\varphi(\vec{k}, \omega) = \frac{e}{2\pi^2} \frac{\delta(\omega - \vec{k} \cdot \vec{v})}{k^2 - \omega^2/c^2}.$$

Inserting both equations in Eq.(46) leads to the representation of the electric field in the frequency/wave number domain,

$$\vec{E}(\vec{k}, \omega) = i \frac{e}{2\pi^2} \frac{\omega \vec{v} - \vec{k} c^2}{k^2 c^2 - \omega^2} \, \delta(\omega - \vec{k} \cdot \vec{v}) \tag{47}$$

Eq. (47) is a common representation of the particle electric field (see e.g. Ref. [25]) and is often used in situations where the form of the surrounding is of minor interest, as for example in the case of parametric X–rays where only the momentum transfer from the crystal lattice to the virtual photon field is considered [34]. Sometimes in literature slightly different representations are found [35], exploiting the property of the δ–function:

$$\vec{E}(\vec{k}, \omega) = i \frac{e}{2\pi^2} \frac{\omega/c^2 \vec{v} - \vec{k}}{k^2 - (\vec{k} \cdot \vec{v})^2/c^2} \, \delta(\omega - \vec{k} \cdot \vec{v}),$$

or if without loss of generality the direction of particle motion is considered to be in z–direction, i.e. $\vec{v} = v \hat{e}_z$. As consequence it follows that $\omega = \vec{k} \cdot \vec{v} = k_z v$ resp. $k_z = \omega/v$. Then Eq.(47) is rewritten in the following form [35]

$$\vec{E}(\vec{k}, \omega) = i \frac{e}{2\pi^2} \frac{\omega/c^2 \vec{v} - \vec{k}}{k_x^2 + k_y^2 + \alpha^2} \, \delta(\omega - \vec{k} \cdot \vec{v}) \tag{48}$$

$$\text{with} \qquad \alpha^2 = \frac{\omega^2}{\gamma^2 v^2}.$$

This representation of the particle electric field is the basis for the following calculations.

In the case of OTR and ODR the field as function of the wave number is of minor interest because it is the shape of the target which has to be taken into account. Therefore a representation of the particle field in the space/frequency domain has to be derived. Rewriting the numerator in Eq.(48) and performing the Fourier back–transform leads to

$$\vec{E}(\vec{r}, \omega) = -i \frac{e}{2\pi^2 v} \int d^3\vec{k} \frac{k_x \hat{e}_x + k_y \hat{e}_y + \frac{k_z}{\gamma^2} \hat{e}_z}{k_x^2 + k_y^2 + \alpha^2} \, \delta(\omega/v - k_z) \, e^{i(k_x x + k_y y + k_z z)} . \tag{49}$$

To solve this equation the individual components have to be treated independently. First of all both transverse components are considered which are of the same form. In this case the z integration can be carried out directly, resulting in

$$E_{x,y}(\vec{r}, \omega) = -i \frac{e}{2\pi^2 v} e^{i \frac{\omega}{v} z} \int\limits_{-\infty}^{+\infty} d^2 k_{x,y} \frac{k_x, k_y}{k_x^2 + k_y^2 + \alpha^2} \, e^{i(k_x x + k_y y)} . \tag{50}$$

The wave number integration is carried out independently for both components. Taking into account symmetry considerations and Ref.[27], Eq. 3.723(4) resp. Eq. 3.914 the solution reads

$$E_{x,y}(\vec{r}, \omega) = \frac{e\alpha}{\pi v} e^{i \frac{\omega}{v} z} \frac{x, y}{\sqrt{x^2 + y^2}} \, K_1(\alpha \sqrt{x^2 + y^2}). \tag{51}$$

For the longitudinal component the z integration can be carried out in a similar way, resulting in

$$E_z(\vec{r}, \omega) = -i \frac{e\alpha}{2\pi^2 v \gamma} \, e^{i \frac{\omega}{v} z} \int\limits_{-\infty}^{+\infty} \mathrm{d}^2 k_{x,y} \, \frac{e^{i(k_x x + k_y y)}}{k_x^2 + k_y^2 + \alpha^2}. \tag{52}$$

Again by means of symmetry considerations and Ref.[27], Eq. 3.723(2) resp. Eq. 3.961(2) the solution can be derived:

$$E_z(\vec{r}, \omega) = -i \frac{e\alpha}{\pi v \gamma} \, e^{i \frac{\omega}{v} z} \, \mathrm{K}_0(\alpha \sqrt{x^2 + y^2}). \tag{53}$$

Eqn.(51) and (53) can be combined to represent the particle electric field in a closed form

$$\vec{E}(\vec{r}, \omega) = \frac{e\alpha}{\pi v} \, e^{i \frac{\omega}{v} z} \left(\frac{\mathrm{K}_1(\alpha \sqrt{x^2 + y^2})}{\sqrt{x^2 + y^2}} (x \hat{e}_x + y \hat{e}_y) - \frac{i}{\gamma} \, \mathrm{K}_0(\alpha \sqrt{x^2 + y^2}) \, \hat{e}_z \right) \tag{54}$$

or in cylindrical coordinates with $x = \rho \cos\varphi$ and $y = \rho \sin\varphi$:

$$\vec{E}(\rho, \varphi, z, \omega) = \frac{e\alpha}{\pi v} \, e^{i \frac{\omega}{v} z} \left(\mathrm{K}_1(\alpha \rho) \, \hat{e}_\rho - \frac{i}{\gamma} \, \mathrm{K}_0(\alpha \rho) \, \hat{e}_z \right). \tag{55}$$

The last two equations are exact representations of the particle field, and they are used for example in Ref. [23] as input for a vector electromagnetic theory for transition and diffraction radiation.

However, if an ultra relativistic particle is considered the contribution of the longitudinal component can be neglected due to their γ^{-1} dependency. In this case the Fourier components of the relativistic particle are interpreted as plane electromagnetic waves which are purely radial transverse electric fields (Weizsäcker–Williams approximation or method of virtual photons, c.f. Ref.[25]). In this case the representation of the particle field is described by Eq.(50) resp. Eq.(51). Both equations serve as input for the investigation of the imaging properties of OTR and ODR, see for example Refs.[1, 2].

Restricting to the case of an ultra relativistic particle, a measure for the radial extension of the pseudo photon disc described by Eq.(55) can be defined as weighted average over the disc [36]:

$$\sigma = \frac{\int \mathrm{d}f \, \rho \, E_\rho(\rho, \varphi, z, \omega)}{\int \mathrm{d}f \, E_\rho(\rho, \varphi, z, \omega)} = \frac{\int\limits_0^\infty 2\pi\rho \, \mathrm{d}\rho \, \rho \, E_\rho(\rho, \varphi, z, \omega)}{\int\limits_0^\infty 2\pi\rho \, \mathrm{d}\rho \, E_\rho(\rho, \varphi, z, \omega)} = \frac{\int\limits_0^\infty \mathrm{d}\rho \, \rho^2 \, \mathrm{K}_1(\alpha\rho)}{\int\limits_0^\infty \mathrm{d}\rho \, \rho \, \mathrm{K}_1(\alpha\rho)}$$

According to Ref.[27], Eq. 6.561(16) the result is given by

$$\sigma = \frac{2}{\pi^2} \lambda \beta \gamma \,, \tag{56}$$

or simplified written (with $\beta = 1$), the characteristic radius of the pseudo photon disc amounts

$$\sigma \approx \lambda \gamma \,. \tag{57}$$

Acknowledgmnent

References

[1] A.P. Potylitsyn, in NATO Workshop "*Advanced Radiation Sources and Applications*" (Springer, New York, 2006), pp. 149-163.

[2] D. Xiang, W.-H. Huang, Nucl. Instr. Meth. A**570** (2007) 357.

[3] O.V. Afanasyev, A.B. Baluev, K.I. Gubrienko, E.A. Merker, K. Wittenburg, and I. Krouptchenkow, AIP Conf. Proc. **868** (2006) 534.

[4] V.E. Scarpine, A.H. Lumpkin, and G.R. Tassotto, AIP Conf. Proc. **868** (2006) 473.

[5] L. Wartski et al., J. Appl. Phys. **46** (1975) 3644.

[6] R.B. Fiorito and D.W. Rule, AIP Conf. Proc. **319** (1994) 21.

[7] K. Honkavaara et al., in Proceedings of PAC03, Portland (Oregon), 2003, p.2476.

[8] F. Loehl et al., Phys. Rev. ST Accel. Beams **9** (2006) 092802.

[9] C. Bal, E. Bravin, E. Chevallay, T. Lefèvre, and G. Suberlucq, in Proceedings of DIPAC03, Mainz, 2003, p.95.

[10] P. Catravas et al., in Proceedings of the PAC99, New York, 1999, p.2111.

[11] The European X–Ray Free–Electron Laser Technical Design Report, DESY 2006-097 (2007).

[12] V.A. Lebedev, Nucl. Instr. Meth. A**372** (1996) 315.

[13] X. Artru, Nucl. Instr. Meth. A**410** (1998) 148.

[14] X. Artru, R. Chehab, K. Honkavaara, and A. Variola, Nucl. Instr. Meth. B**145** (1998) 160.

[15] M. Castellano and V.A. Verzilov, Phys. Rev. ST Accel. Beams **1** (1998) 062801.

[16] V.A. Verzilov, Phys. Lett. A**273** (2000) 135.

[17] J.-C. Denard, P. Piot, K. Capek, and E. Feldl, in Proceedings of the PAC97, Vancouver (Canada), 1997, p.2198.

[18] M. Ross et al., AIP Conf. Proc. **648** (2002) 237.

[19] A.P. Potylitsyn, Nucl. Instr. Meth. B**145** (1998) 169.

[20] N.A. Potylitsina–Kube and X. Artru, Nucl. Instr. Meth. B**201** (2003) 172.

[21] H. Backe et al., Z. Phys. A**349** (1994) 87.

[22] H. Backe et al., AIP Conf. Proc. **389** (1997) 57.

[23] A.G. Shkvarunets and R.B. Fiorito, Phys. Rev. ST Accel. Beams **11** (2008) 012801.

[24] D.V. Karlovets and A.P. Potylitsyn, Nucl. Instr. and Meth. in Phys. Res. B (2008), doi: 10.1016/j.nimb.2008.02.014.

[25] M.L. Ter–Mikaelian, *High–Energy Electromagnetic Processes in Condensed Media* (Wiley Interscience, New York, 1972).

[26] J.W. Goodman, *Introduction to Fourier Optics*, 3rd ed. (Roberts & Company Publishers, Colorado, 2004).

[27] I.S. Gradshteyn and I.M. Ryzhik, *Table of Integrals, Series, and Products*, 5th ed. (Academic Press, New York, 1994).

[28] M.A. Abramowitz and I. Stegun, *Pocketbook of Mathematical Functions* (Verlag Harri Deutsch, Thun - Frankfurt/Main, 1984).

[29] Basler A301f Camera´s User Manual, Document ID Number DA00044803 (2002), Basler Vision Technologies.

[30] J.M. Geary, *Introduction to Lens Design* (Willmann–Bell, Inc., Richmond, Virginia, 2002).

[31] V.E. Scarpine, C.W. Lindenmeyer, G.R. Tassotto, and A.H. Lumpkin, in Proceedings of PAC05, Knoxville (Tennessee), 2005, p. 2381.

[32] LINOS Photonics GmbH & Co. KG, `http://www.linos.com/pages/home.html`.

[33] `http://www.zemax.com`.

[34] A. Caticha, Phys. Rev. A**40** (1989) 4322.

[35] B.M. Bolotovskii and G.V. Voskresenskii, Soviet Phys. Uspekhi **9** (1966) 73.

[36] D. Xiang, W.-H. Huang, Nucl. Instr. Meth. B**248** (2006) 163.